Stable Silicon Anodes by Molecular Layer Deposited Artificial Zincone Coatings

14 authors, including:

Mu Tiansheng
Harbin Institute of Technology
16 PUBLICATIONS **432** CITATIONS

SEE PROFILE

Yang Zhao
The University of Western Ontario
146 PUBLICATIONS **7,239** CITATIONS

SEE PROFILE

Changtai Zhao
The University of Western Ontario
92 PUBLICATIONS **3,898** CITATIONS

SEE PROFILE

Shuaifeng Lou
Harbin Institute of Technology
66 PUBLICATIONS **1,579** CITATIONS

SEE PROFILE

Some of the authors of this publication are also working on these related projects:

Li Protection View project

Rational Design Carbon-based Nanohybrids for Energy Storage and Conversion View project

Stable Silicon Anodes by Molecular Layer Deposited Artificial Zincone Coatings

Tiansheng Mu, Yang Zhao, Changtai Zhao, Nathaniel Graham Holmes, Shuaifeng Lou, Junjie Li, Weihan Li, Mengxue He, Yipeng Sun, Chunyu Du, Ruying Li, Jiajun Wang, Geping Yin,* and Xueliang Sun*

A stable interface between silicon anodes and electrolytes is vital to realizing reversible electrochemistry cycling for lithium-ion batteries. Herein, a zincone polymer coating is controllably deposited on a silicon electrode using the molecular layer deposition to serve as an artificial solid electrolyte interphase (SEI). Enhanced electrochemical cycling depends on the thickness of zincone coating. The optimal zincone coating of ≈3 nm markedly improves the lithium storage performance of silicon anodes, resulting in a high reversible capacity (1741 mA h g^{-1} after 100 cycles at 200 mA g^{-1}), outstanding cycling stability (1011 mA h g^{-1} after 500 cycles), and superior rate capability (1580 mA h g^{-1} at 2 A g^{-1}). Such remarkable electrochemical reversibility stems from the in situ conversion of the zincone coating and a zincone-driven thin lithium fluoride (LiF)-rich SEI, which endow the silicon electrode with superior electron/ion transport and structural stability. Meanwhile, the zincone coating demonstrates good compatibility with ether-based electrolytes (893 mA h g^{-1} after 200 cycles, 970 mA h g^{-1} at 5 A g^{-1}). Additionally, in situ conversion of artificial zincone coating also opens a door for constructing a functional interface on other electrode surfaces, such as lithium/sodium metal.

1. Introduction

The development of electric vehicles and large-scale energy storage equipment has resulted in increasingly demanding requirements for lithium-ion batteries (LIBs) in terms of energy density and cycle life.[1] Commercial LIBs based on traditional graphite and lithium cobalt oxide are approaching the limit of their ability to meet the market demand for high energy density devices.[2] Seeking alternative electrode materials with high capacity is one way to improve the energy density of LIBs. Considering anode materials, silicon is considered as one of the most competitive candidates due to a high theoretical capacity, ease of production, low cost, and low environmental impact.[3] However, the volume swells/shrinks (≈400%) and continuous interfacial reaction during battery operation seriously hinders the commercialization of silicon anodes.[4] This huge volume fluctuation leads to the mechanical fracture of silicon particles, causing exposing more fresh silicon interface to the electrolyte. In turn, the reformation of the unstable solid electrolyte interphase (SEI) is exacerbated, causing poor Coulombic efficiencies, fast capacity decay, and deteriorative rate capability.[5] The abovementioned issues have resulted in the stagnation of the development of silicon anodes for the past ten years.

Numerous strategies have been proposed to relieve the volume effect and improve the structural stability of silicon anodes including nanostructuring,[6] buffer matrix composites,[7] heterogeneous doping,[8] multifunctional binders,[2,9] and electrolyte additives.[10] Previous reports have shown that silicon nanoparticles smaller than 150 nm can better relieve stress caused by volume change.[11] Composites with nano-size silicon are therefore expected to stabilize silicon anodes. Such composites typically employ inactive/active buffer coatings, which have been theorized to act as protective layers to prevent unwanted side reactions between silicon and liquid electrolytes during cycling.[12] Commonly developed carbonaceous coatings and oxide coatings have been proposed and notably improve the cyclability of silicon anodes. However, they still have limitations including the catalytic effect of carbon on the decomposition of liquid electrolytes and the poor toughness of oxides, which severely restricts the long-stem electrochemical reversibility of silicon anodes.[12,13] Consequently, serious challenges have yet to be overcome in the surface coating engineering of silicon anodes.

Artificial polymer coatings have attracted widespread attention due to their flexibility, toughness, and graftable chemistry.[14] The molecular layer deposition (MLD) paves the way for precisely controlled synthesis of polymers through self-limited

T. Mu, Dr. S. Lou, M. He, Dr. C. Du, Dr. J. Wang, Prof. G. Yin
MIIT Key Laboratory of Critical Materials Technology for New Energy Conversion and Storage
School of Chemistry and Chemical Engineering
Harbin Institute of Technology
Harbin 150001, China
E-mail: yingeping@hit.edu.cn
T. Mu, Dr. Y. Zhao, Dr. C. Zhao, N. Holmes, J. Li, Dr. W. Li, M. He, Y. Sun, R. Li, Prof. X. Sun
Department of Mechanical and Materials Engineering
University of Western Ontario
London, Ontario N6A 5B9, Canada
E-mail: xsun9@uwo.ca

reactions.[15] Ban's group developed a so-called alucone coating on a silicon electrode, and the alucone coating with good mechanical properties promotes a significant improvement in cyclability of silicon anode.[16] However, the understanding that the physical mechanical restraint improves electrochemical cycling is insufficient. And the mechanisms behind the electrochemical evolution of the MLD coating still remain unknown, limiting our ability for the efficient design of artificial surface coatings. In addition to this, cyclic reversibility and rate capability also demonstrate room for improvement.

Herein, a zincone coating, for the first time, was controllably deposited on silicon electrodes by MLD. The optimized zincone coating greatly expands electrochemical cycling lifespan, which origins from in situ conversion of artificial zincone coating and a zincone-induced thin LiF-rich SEI. Specifically, the lithium ion storage performance includes outstanding cycling stability (1011 mA h g^{-1} after 500 cycles) and rate capability (1580 mA h g^{-1} at 2 A g^{-1}). Also, the zincone coating obviously reduces the transfer impedance and effectively stabilizes the volume change of the silicon electrode. Meanwhile, the zincone coating displays superior compatibility with ether-based electrolytes. In additional, in situ electrochemical conversion of zincone coating also provides a good idea for constructing the functional interface on other electrode surfaces (e.g., Li metal anode).

2. Results and Discussion

Figure 1a demonstrates a schematic diagram of the zincone coated silicon electrode by MLD. The zincone coating was deposited on the silicon electrode instead of silicon nanoparticles in order to keep electron/ion unobstructed transport. Previous reports have proven MLD coatings on the electrodes to be more advantageous than MLD coating silicon nanoparticles directly.[15b,17] The zincone coating was deposited by self-limiting surface chemistry between ethylene glycol (EG) and diethylzinc (DEZ), which achieves control at the molecular level.[18] DEZ first reacts with silanol on the surface of silicon and leaves an ethyl zinc terminated surface. The zinc ethyl continues to react with the alcoholic hydroxyl group of the EG. The second alcoholic hydroxyl group in the EG then continues reacting with the DEZ. These steps represent one MLD cycle. The zincone coating thickness can be controlled by the number of reaction cycles. Here, silicon electrodes with 10, 25, and 50 cycles of zincone coating were prepared. These electrodes are denoted as Si@10-ZC, Si@25-ZC, and Si@50-ZC, respectively.

Physical characterization was carried out to verify the presence of the zincone coating, measure coating thickness, and examine electrode morphology. The Si@10-ZC electrode was used for physical characterization due to its optimal electrochemical performance. The X-ray diffraction (XRD) test results
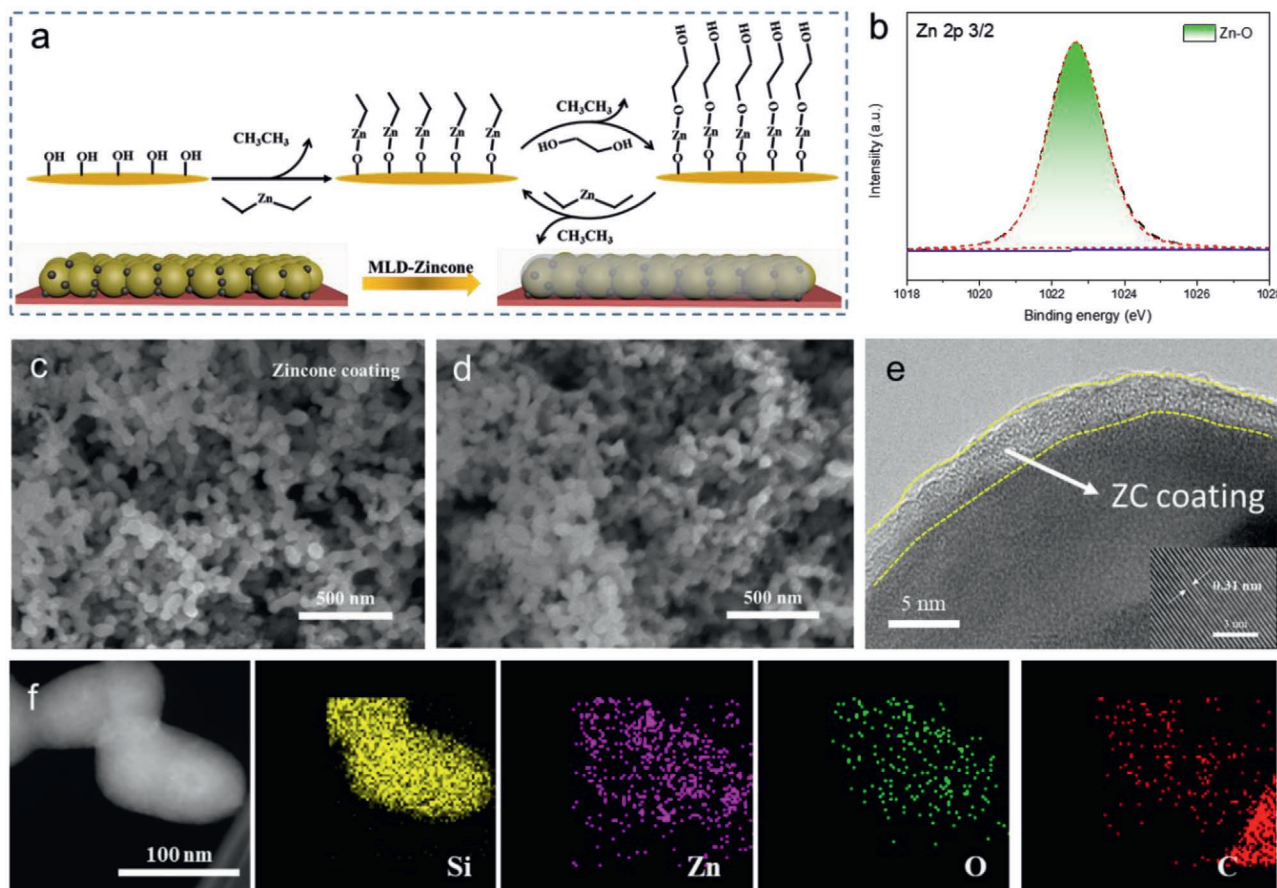

Figure 1. a) A schematic diagram of a MLD-zincone coated silicon electrode; b) XPS spectrum of Zn 2p$_{3/2}$; SEM images of c) the Si@10-ZC electrode; d) the pristine silicon electrode; e) HRTEM image with inset showing the lattice fringe; f) STEM-EDS elements mappings for Si@10-ZC.

of electrodes are displayed in Figure S1, Supporting Information. Specifically, the three diffraction peaks at ≈28.4°, ≈47.1°, and ≈56.0° are attributed to crystal silicon, corresponding to (111), (220), and (311) crystal planes of silicon lattice (JCPDS No. 27-1402), respectively.[4] The diffraction peaks of the copper foil were also detected since the electrodes were directly used as the test objects. The three peaks at ≈43.2°, 50.2°, and ≈74.0° belong to metal copper, corresponding to (111), (200), and (220) crystal planes of copper.[19] The XRD pattern shows no additional peak for the Si@10-ZC electrode compared to the pristine silicon electrode, indicating that the zincone coating is amorphous.[20] As shown in Figure S2, Supporting Information, X-ray photoelectron spectroscopy (XPS) survey spectra exhibit an obvious zinc peak for Si@10-ZC electrode, indicating the presence of a zincone coating.[18,21] In Figure 1b, the peak at ≈1022.5 eV in the Zn $2p_{3/2}$ spectrum corresponds to the Zn—O bond in the zincone.[22] There is no visible difference between the Si@10-ZC electrode and the pristine silicon electrode in the scanning electron microscope (SEM) images in Figure 1c,d, indicating a conformal and ultrathin zincone coating. Simultaneously, the Si@25-ZC and Si@50-ZC electrodes show a similar conformal morphology in Figure S3, Supporting Information. The uniform distribution of zincone coatings can be observed on the electrode scale by the zinc mapping, and the corresponding EDS spectrum indicates the presence of zincone in Figure S4, Supporting Information. Transmission electron microscope (TEM) was characterized to determine the thickness of the zincone coating for the Si@10-ZC electrode. As shown in Figure S5, Supporting Information, the silicon particle size is smaller than 100 nm. And the diffraction ring of silicon nanoparticles is consistent with polysilicon.[23] The thickness of the zincone coating is ≈3 nm as shown in Figure 1e. The inset shows a lattice spacing of 0.31 nm, corresponding to the (111) crystal plane of silicon.[24] In Figure 1f, the relevant element EDS mappings demonstrate the uniform distribution of zincone coating on silicon nanoparticles, which further confirms the identification of zincone coating on the silicon electrode.

The lithium storage performance was characterized using lithium metal as a counter electrode as shown in **Figure 2**. The initial three charge–discharge curves of the Si@10-ZC electrode are shown in Figure 2a. The first discharge and charge specific capacities are 3386 and 2710 mA h g⁻¹, respectively. The corresponding initial Coulombic efficiency is up to 80%, a significant improvement over the pristine silicon electrode (73%) in Figure S6, Supporting Information. This mainly is due to the zincone coating preventing direct contact between silicon nanoparticles and the liquid electrolyte.[4,25] Besides, there is no obvious capacity attenuation during the initial three cycles, demonstrating outstanding electrochemical reversibility.[26] The cyclic voltammetry (CV) curves of the Si@10-ZC electrode are indicated in Figure 2b. The broad peak at ≈0.9 V corresponds to the SEI information during the first lithiation process,[27] and the peak at ≈0.5 V corresponds to the reaction between the zincone and lithium. The next CV cycles demonstrates electrochemical behavior characteristic of silicon anode and are consistent with the CV behavior of pristine silicon electrode in Figure S7, Supporting Information.

The rate capability and cycling stability of samples were tested to explore the best electrochemical stability. Obviously,

the Si@10-ZC electrode shows the best lithium storage performance. The Si@25-ZC and Si@50-ZC electrodes also deliver enhanced electrochemical stability compared to the pristine silicon electrode, especially in terms of rate capability. Understandably, the optimal coating thickness is a trade-off between lithium ion transport ability and structural stability. The Si@10-ZC electrode shows obviously improved rate capability in Figure 2c. Even at 2 A g⁻¹, a high specific capacity of 1580 mA h g⁻¹ is achieved, compared to a specific capacity of only 416 mA h g⁻¹ for the pristine silicon electrode. The corresponding charge and discharge curves at different current densities are displayed in Figure 2d. For the Si@10-ZC electrode, a high reversible capacity of 1741 mA h g⁻¹ is maintained after 100 cycles at 200 mA g⁻¹ in Figure 2e. As a comparison, the specific capacity of the pristine silicon electrode remains at only 563 mA h g⁻¹ after 100 cycles. Meanwhile, the corresponding Coulombic efficiency curves of Si@10-ZC and pristine silicon electrode are shown in Figure S8, Supporting Information. For Si@10-ZC electrode, the Coulombic efficiencies soon increased to over 97.5% after five cycles, and the curve keeps stable during cycling, showing the artificial zincone coating promotes the formation of a stable SEI interface. As a contrast, the pristine silicon electrode shows the relatively low Coulombic efficiencies during the initial 70 cycles, and the curve shows obvious fluctuations due to an unstable interface chemistry. The long-stem cycling stability of samples was characterized at 1 A g⁻¹ as shown in Figure 2f. The activation current density in the initial two cycles is 100 mA g⁻¹. For Si@10-ZC electrode, a high reversible capacity of 1011 mA h g⁻¹ is retained after 500 cycles, illustrating the impressive cycling stability. And this cycling curve shows the slight fluctuation within first 40 cycles, which maybe caused by temperature disturbances.[28] In contrast, the pristine silicon electrode demonstrates a rapid capacity decline, and the battery fail soon after 100 cycles. Meanwhile, to demonstrate the better flexibility mechanical buffer of the zincone coating, a comparative atomic layer deposition (ALD)-zinc oxide (ZnO) coated silicon electrode, denoted as Si@ZnO electrode, was prepared and characterized. The Si@ZnO electrode displays the poor cycling stability compared to the Si@10-ZC electrode at 1 A g⁻¹. A specific capacity of only 508 mAh g⁻¹ is obtained after 360 cycles. Also, the Si@ZnO electrode exhibits a relatively poor rate capacity as shown in Figure S9, Supporting Information. At 2 A g⁻¹, the reversible capacity is 1052 mAh g⁻¹. Therefore, the zincone coating greatly improves the electrochemical stability of silicon anodes in the carbonate-based electrolyte.

Silicon-sulfur batteries have attracted much attention due to their high energy density.[29] Sulfur cathodes must be paired with ether-based electrolytes. Therefore, the lithium storage performance of silicon anodes in ether-based electrolytes is of great importance. The electrochemical performance of the Si@10-ZC electrode in ether-based electrolytes was tested. The first charge–discharge curve is displayed in Figure S10, Supporting Information, showing an initial Coulombic efficiency of 78%. The improved rate capability is shown in Figure 2g. Specifically, a high reversible capacity of 970 mA h g⁻¹ is maintained at 5 A g⁻¹. In contrast, the specific capacity of the pristine silicon electrode is almost zero at the same current density. Cycling stability shows a significant improvement with a specific capacity of 893 mA h g⁻¹ after 200 cycles at 1 A g⁻¹ in
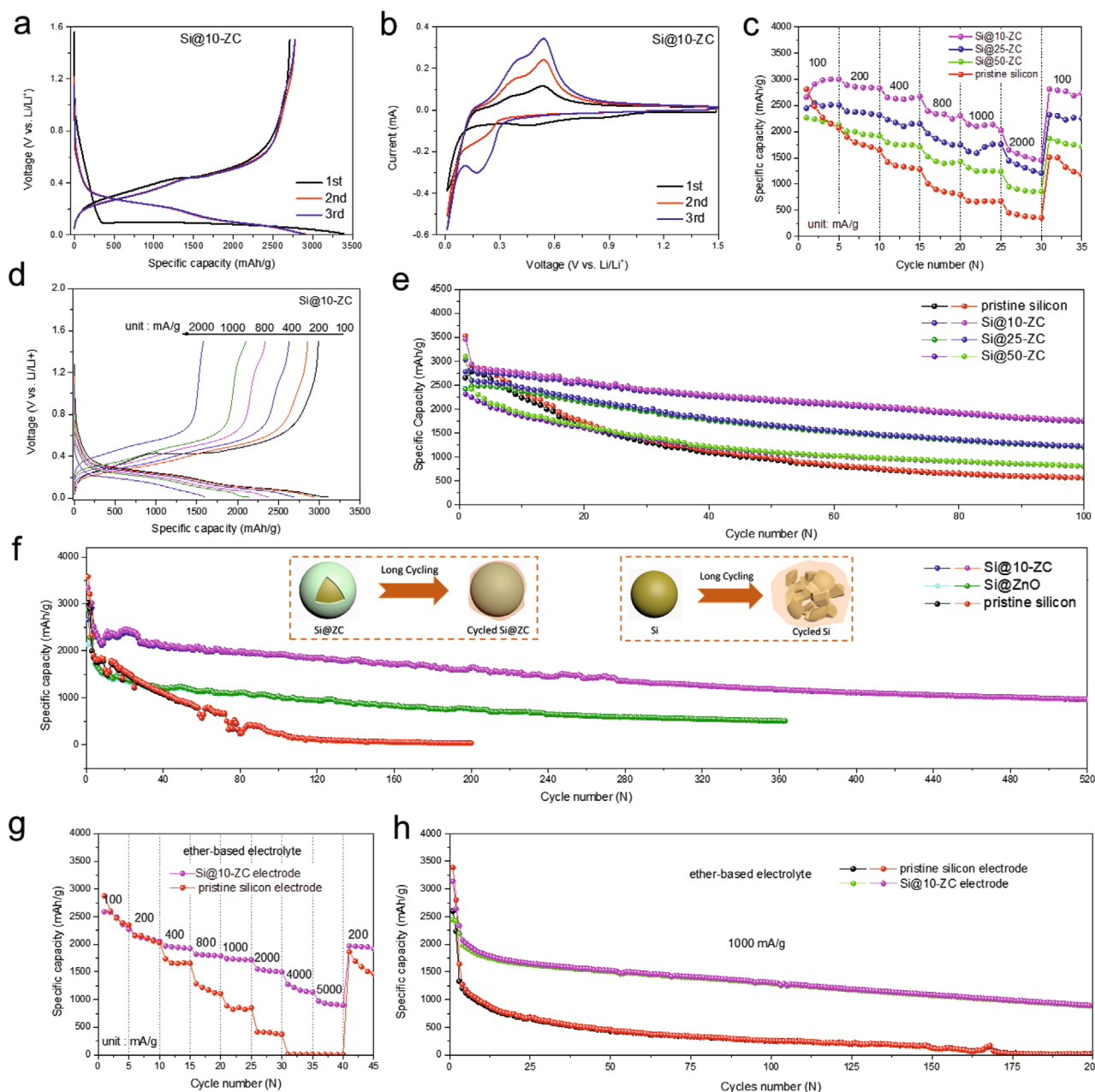
**ADVANCED
SCIENCE NEWS**

www.advancedsciencenews.com

**ADVANCED
FUNCTIONAL
MATERIALS**

www.afm-journal.de

Figure 2. Electrochemical performance a) the charge–discharge curves of Si@10-ZC; b) the CV curves of Si@10-ZC; c) rate performance; d) charge–discharge curves at different current densities; e) cycling performance at 200 mA g^{-1}; f) cycling performance at 1 A g^{-1}. In ether-based electrolytes g) the rate performance; h) the cycling performance at 1 A g^{-1}.

Figure 2h. In contrast, the pristine silicon electrode fails after 160 cycles. Therefore, whether in the carbonate-based electrolyte or the ether-based electrolyte, the zincone coating significantly improves the cycling stability and rate capability of silicon anodes. Furthermore, the electrochemical performance of Si@10-ZC is even better than some silicon-carbon composite anodes and some advanced anode materials (such as metal oxides and sulfides) in terms of cycling capacity and rate capability.[30]

In order to fundamentally understand the improved lithium storage performance, the electrochemical evolution of zincone

coatings needs to be recognized. Previous reports pay little attention to this point. A CV test of 50 cycles zincone film on a copper foil was conducted as shown in **Figure 3**a. There are two obvious peaks at ≈0.5 and ≈1.0 V during the first negative scan, which corresponds to the lithiation reaction between zincone and lithium and is consistent with the results in Figure 2b. The coincidence of the subsequent CV cycles shows the electrochemical stability of the zincone coatings. The evolution mechanisms of zinc (Zn) during the first cycle were further explored using ex situ X-ray absorption near edge structure (XANES). Si@10-ZC electrodes at different potentials shown in Figure 3b
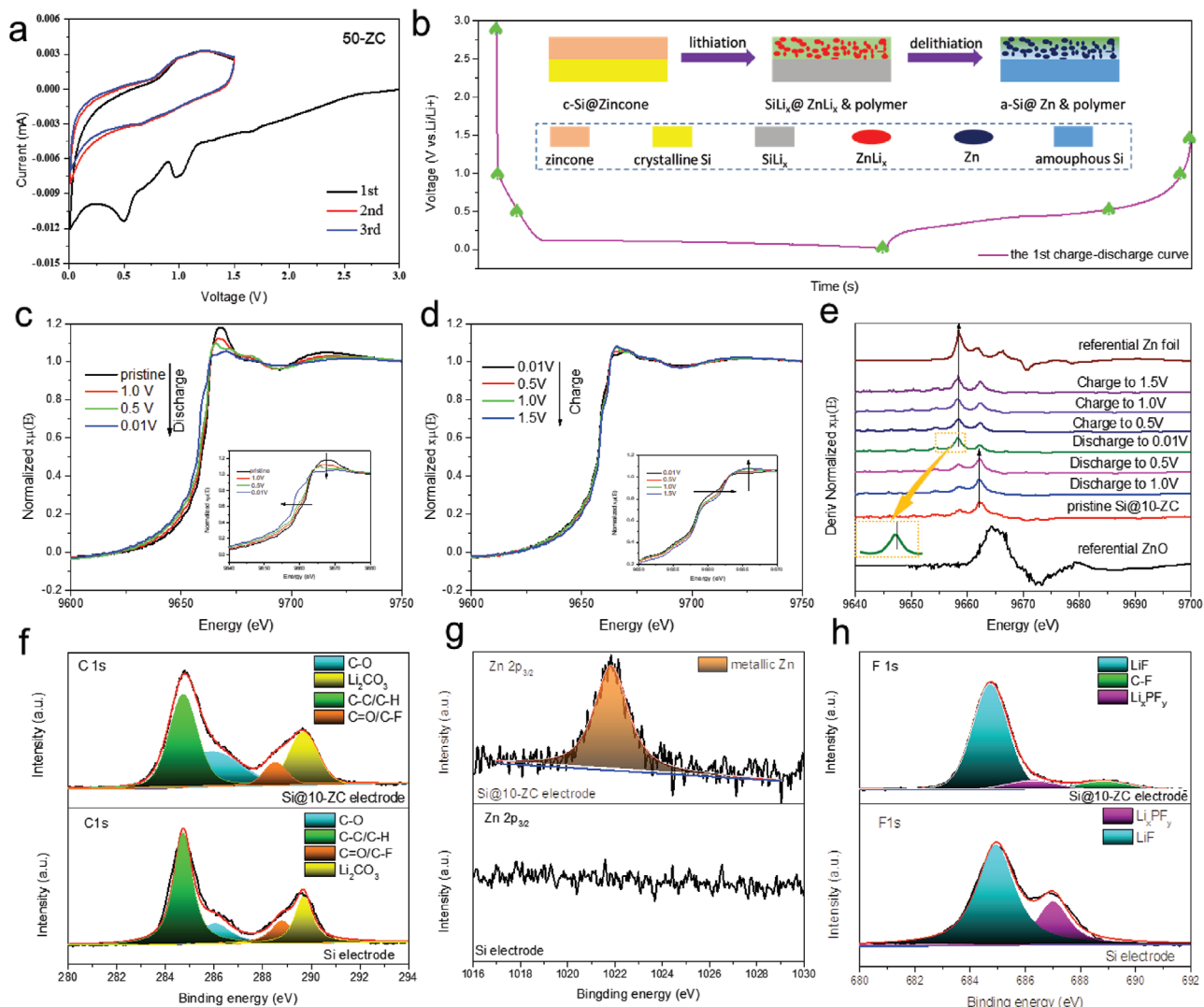
Figure 3. a) CV curves of zincone film; ex situ Zn K-edge XANES tests b) test points at different potentials; c) during lithiation; d) during delithiation; inset is part showing enlarged region. e) The corresponding differential curves of the XAS spectra at different potentials. XPS spectra after 50 cycles f) C 1s; g) Zn 2p$_{3/2}$; h) F 1s.

were prepared according to the CV curve of the zincone film in Figure 3a. The corresponding X-ray absorption spectroscopy (XAS) spectra taken during lithiation are displayed in Figure 3c. During lithiation, the Zn K-edge moves to a lower energy, and the peak intensity decreases, indicating the reduction of zinc.[31] During delithiation, the Zn K-edge moves to a higher energy, and the peak intensity increases in Figure 3d, indicating the electronic loss of Zn. Figure 3e shows the derivative curves of the XAS absorption spectra, and the position of the strongest peak can reflect valence state of zinc. The Zn K-edge absorption spectra for the reference ZnO powder and Zn foil are shown in Figures S11 and S12, Supporting Information, respectively. When the lithiation reaches 0.01V, metallic Li$_x$Zn alloy is formed, evidenced by the lower peak position than the Zn foil. During the subsequent delithiation process from 0.01 to 1.5 V, metallic zinc is formed in the silicon electrode. The good conductivity of metallic zinc (Zn or Li$_x$Zn) accelerates charge transfer and promotes faster reaction kinetics. Consequently,

the ex situ XAS study helps to further clarify the evolution of the zincone coating during charge and discharge and explain the improvement in electrochemical performance.

As an artificial SEI, conformal zincone coatings definitely participate in the formation of SEI, which is known to be key determinants of battery performance. The effect of the zincone coating on SEI composition was explored by XPS. In Figure 3f, the C 1s spectrum of Si@10-ZC reveals a reduction in the proportion of inorganic lithium carbonate (Li$_2$CO$_3$), indicating that the zincone coating inhibits the formation of insoluble electrolyte reduction products. A comparison shows an increase in organic polymers containing C−O and C=O bonds.[32] These polymers are most likely transformation products of the zincone coating during cycling and play an important role in buffering the volume expansion and maintain the structural stability of silicon electrodes. In the Zn 2p$_{3/2}$ spectrum, the peak at ≈1021.8 eV shifts to a low energy compared to the peak associated with zincone as shown in Figure 3g, suggesting the

**ADVANCED
SCIENCE NEWS**

www.advancedsciencenews.com

**ADVANCED
FUNCTIONAL
MATERIALS**

www.afm-journal.de

formation of metallic zinc from the reduction of zincone.[22] This is consistent with the ex situ XAS test results. The Zn $2p_{3/2}$ spectrum shows no peak for the pristine silicon electrode. According to the discussion above, in situ conversion of zincone coatings are as described in the inset of Figure 3b.

For the F 1s spectrum, the peak intensity corresponding to lithium fluoride (LiF) increases compared to the pristine silicon electrode in Figure 3h, suggesting increased LiF content. It is well-known that LiF has high elastic modulus and ionic conductivity, two essential properties for achieving a stable SEI.[33] The increased LiF content is mainly because the zincone-derivatives inhibit the decomposition of lithium salts, leading to a decrease of Li_xPF_y. In other words, the zincone coating can promote the enrichment of LiF on silcon electrode. Simultaneously, it is also possible that the zincone-derivatives change the reaction path of the SEI formation to favoring the production of more LiF. However, further work is required to validate this hypothesis. Noticeably, the LiF and metallic zinc improve the ionic and electronic conductivity of the electrode, while the zincone-drived polymers buffer the volume change of the silicon, resulting in improved cycling stability and rate performance.

The effect of the zincone coatings on the structure and thickness of the SEI was investigated using the time-of-flight secondary ion mass spectrometry (TOF-SIMS). Porous silicon electrodes have similar SEI structure to silicon film electrodes. The SEI thickness is determined by finding the point, at which the derivative of the silicon or LiF signals with respect to sputter depth goes to zero. Si and LiF produce Si^- and LiF_2^- ion signals, respectively. Zincone-drived metallic zinc produces a ZnO^- ion

signal while Li_xPF_y and residual lithium salt produce a PF_6^- ion signal. Distinctly, much less time is required for the signal derivative to reach zero with the Si@10-ZC electrode ($\approx$80 s) compared to the pristine silicon electrode (>300 s) as shown in **Figure** 4a,b, indicating that the Si@10-ZC electrode possesses a thinner SEI. This is likely one of the reasons for the smaller SEI resistance (R_{SEI}) of the Si@10-ZC electrode. Furthermore, the ZnO^- signal remains constant below the SEI, indicating a uniform distribution of metallic zinc in the silicon electrode.

Figure 4c,d demonstrates the TOF-SIMS secondary ion images after 20 and 220 s of sputtering the Si@10-ZC electrode, respectively. A weak silicon signal in Figure 4c indicates that the surface of the Si@10-ZC electrode is covered by the SEIs. After 220 s of sputtering, Figure 4d shows the silicon signal reaching saturation, indicating that the silicon is completely exposed. Meanwhile, evenly distributed metallic zinc is also observed in the electrode. Interestingly, the LiF shows the spotted aggregation, which may be caused by the porous electrode structure. In Figure 4e, the corresponding 3D reconstructions more vividly reflect the electrode structure. Metallic zinc is uniformly distributed, and the columnar LiF is distributed through the electrode. This distribution plays an important role in promoting electron/ion transport in silicon electrodes.

In order to further verify the above-mentioned experimental results, the electrochemical impedance spectroscopy (EIS) measurements were carried out for the Si@10-ZC and pristine silicon electrodes after 60 cycles. Before cycling, the EIS spectra of both the Si@10-ZC and pristine silicon electrode show one semicircle and one straight line in Figure S13, Supporting Information. After cycling, the EIS spectra show two
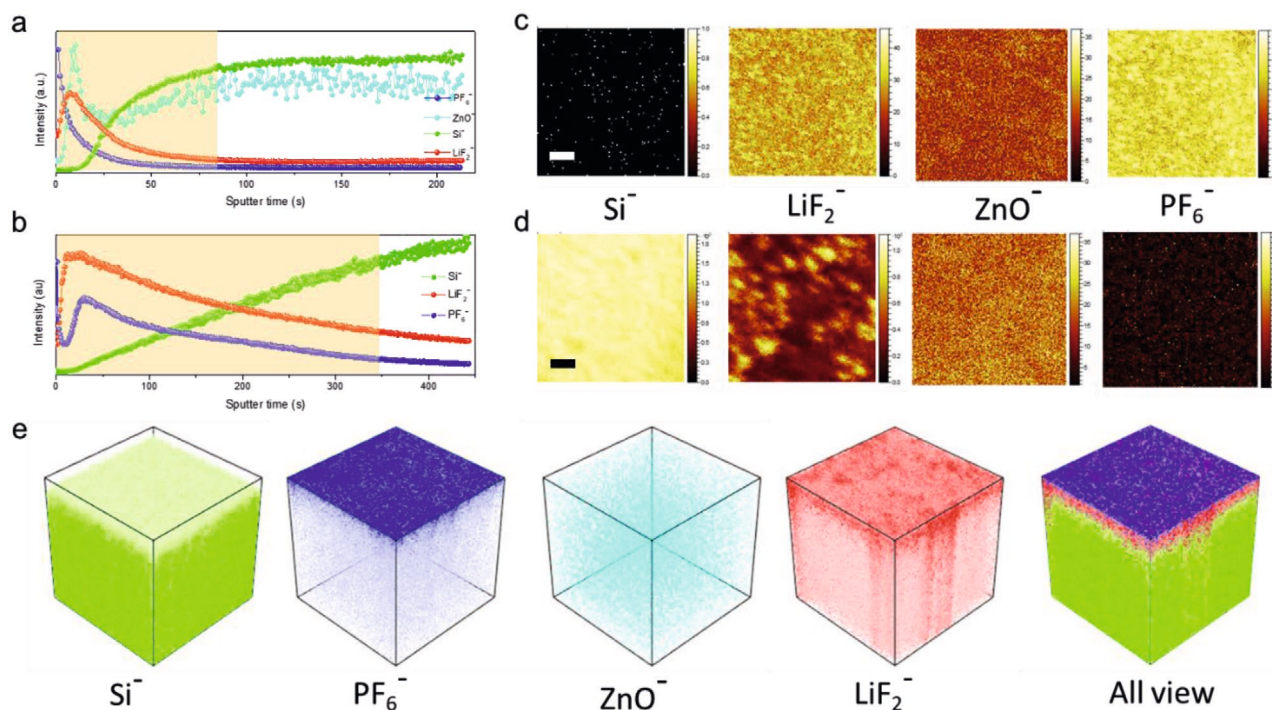

Figure 4. Depth profile of various secondary ion species obtained by sputtering after 80 cycles. a) The Si@10-ZC electrode; b) the pristine silicon electrode. TOF-SIMS secondary ion images of the Si@10-ZC electrode c) after sputtering for 20 s; d) after sputtering for 220 s (the bar is 20 µm). e) 3D reconstructions of the sputtered volume corresponding to the depth profiles in Figure 4a.
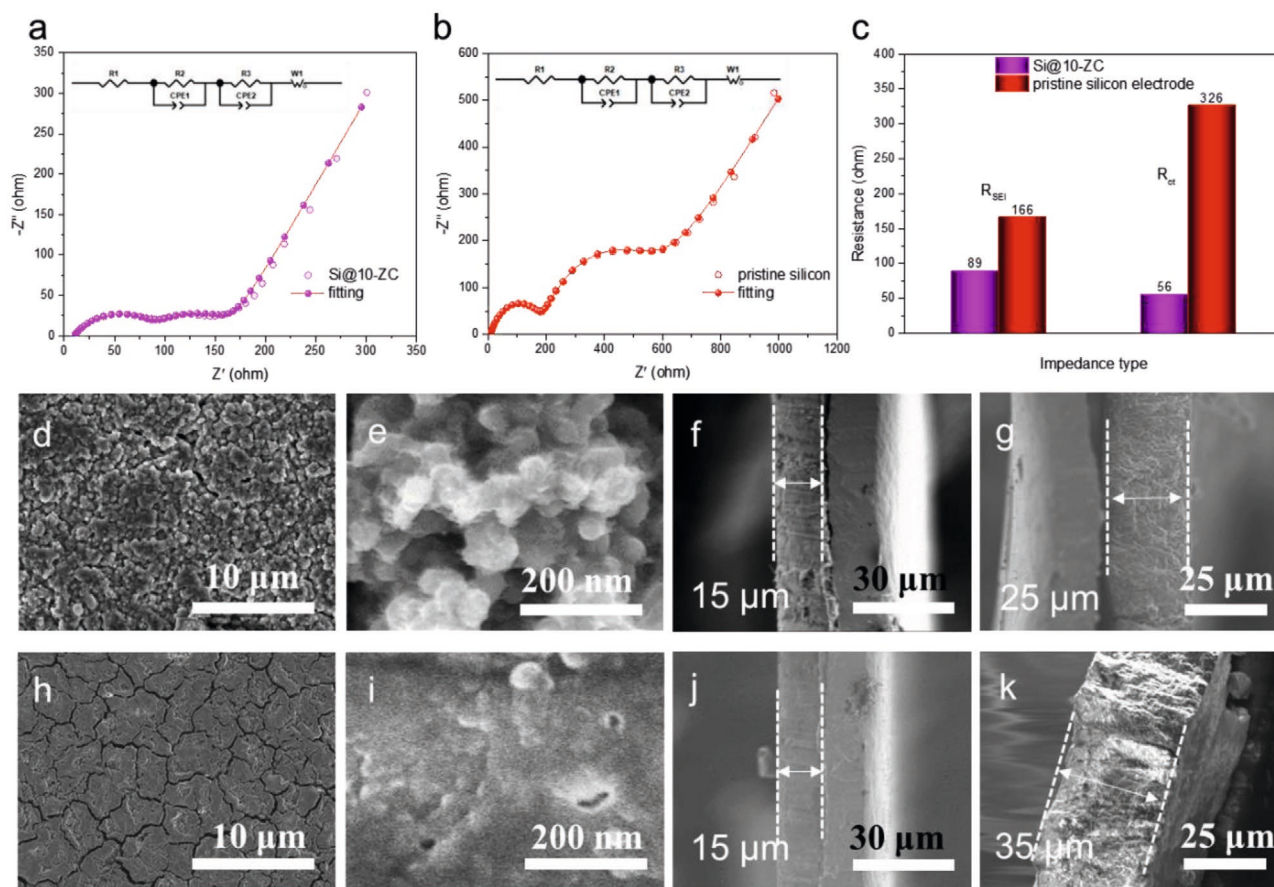
**ADVANCED
SCIENCE NEWS**

www.advancedsciencenews.com

**ADVANCED
FUNCTIONAL
MATERIALS**

www.afm-journal.de

Figure 5. EIS testing after 60 cycles of a) the Si@10-ZC electrode; and b) the pristine silicon electrode; c) a comparison of fitted R_{SEI} and R_{ct}; top-view SEM images after 60 cycles and the corresponding enlarged image of d,e) the Si@10-ZC electrode; and h,i) the pristine silicon electrode. Cross-sectional SEM images before and after 60 cycles of f,g) the Si@10-ZC electrode; and j,k) the pristine silicon electrode.

semicircles in the high frequency region and one straight line in the low frequency region as shown in **Figure 5**a,b, representing the SEI impedance (R_{SEI}), the charge transfer impedance (R_{ct}), and the lithium ion diffusion in the electrode, respectively.[26] The inset is the corresponding equivalent circuit. The R_{SEI} and the R_{ct} of the Si@10-ZC electrode are significantly smaller than that of the pristine silicon electrode. The values obtained by fitting are shown in Figure 5c. The straight line of the Si@10-ZC electrode shows a larger slope than that of the pristine silicon electrode, indicating faster lithium ion diffusion dynamics.[34] The reduced resistance (R_{SEI} and R_{ct}) and accelerated lithium ion diffusion benefit from the stable interface comprised of zincone-derivatives (metallic zinc and polymers) and LiF-dominated SEIs.

The morphology of the electrodes was examined from a top view and cross-sectional view obtained by SEM. The Si@10-ZC electrode displays an intact structure with no obvious cracking after 60 cycles in Figure 5d. Upon closer inspection, the complete silicon nanoparticles can be clearly observed in Figure 5e, indicating that the zincone coating enables the structural stability of silicon nanoparticles during cycling. Additionally, a hairy layer can be observed on the silicon nanoparticles. In contrast, the pristine silicon electrode shows numerous cracks in Figure 5h, and silicon nanoparticles have been covered by a

much thicker SEI in Figure 5i. Additionally, Figure 5f,g is the cross-sectional SEM images of Si@10-ZC electrode before and after cycling, respectively. Figure 5j,k is the cross-sectional SEM images of pristine silicon electrode before and after cycling, respectively. A comparison reveals that the thickness change of the Si@10-ZC electrode before and after cycling was significantly reduced (66%) compared to that of the pristine silicon electrode (133%). Therefore, the zincone coating enhances the structural stability and integrity of the silicon electrode, further enabling improved cycling stability and rate capability.

To test the viability of the Si@10-ZC electrode in practical cells, LiFePO$_4$//Si@10-ZC cells were assembled and tested. A schematic diagram of the LiFePO$_4$//Si@10-ZC cell is shown in Figure S14a, Supporting Information. The initial two charge–discharge curves of the cell are shown in Figure S14b, Supporting Information. The first cycle Coulombic efficiency is 70%, which might be improved through prelithiation in future work. The full cell shows good rate capability with a specific capacity of 90 mA h g^{-1} at 1 C in Figure S14c, Supporting Information. A specific capacity of 110 mA h g^{-1} is maintained after 100 cycles at 0.4 C as shown in Figure S14d, Supporting Information, displaying good cycling stability and suggesting the feasibility of using the Si@10-ZC electrodes for practical LIBs.

ADVANCED
SCIENCE NEWS
www.advancedsciencenews.com

ADVANCED
FUNCTIONAL
MATERIALS
www.afm-journal.de

3. Conclusion

In summary, we proposed that an artificial zincone coating was controllably deposited on a silicon electrode by MLD. A zincone coating of ≈3 nm greatly boosts the cycling stability and rate capability of silicon anode, which is attributed to in situ electrochemical conversion of zincone coatings and a zincone-induced thin LiF-rich SEI. Zincone-derivatives (metallic zinc and an organic polymer) and dominant LiF act as a flexible mechanical buffer and a stable interface with good electronic and ionic conductivity. Electrochemical results from this work include a high reversible capacity (1741 mA h g^{-1} after 100 cycles at 200 mA g^{-1}), superior cycling stability (1011 mA h g^{-1} after 500 cycles), and remarkable rate capability (1580 mA h g^{-1} at 2 A g^{-1} and 970 mA h g^{-1} at 5 A g^{-1}). Furthermore, the zincone coating is compatible with ether-based electrolytes. Combined with the simple coating synthesis process, the superior properties of this zincone coating open the door to many possibilities for practical applications in silicon anodes.

4. Experimental Section

The Preparation of Zincone Coated Electrodes: The zincone (ZC) coating was directly deposited on silicon electrodes by MLD. Specifically, MLD was conducted using a commercially available Gemstar-8 ALD system (Arradiance, USA), which was connected to an argon-filled glovebox. The electrodes were placed into the chamber and the chamber pumped down to a pressure of ≈400 mTorr. 99.999% Ar (Praxair) was used as a carrier gas at a flow rate of 20 sccm. All depositions were conducted at 120 °C. Zincone films were produced using diethyl zinc (DZ, Zn(C$_2$H$_5$)$_2$) and EG precursors using a pulse–purge–pulse–purge program of 0.01 s/40 s/0.01 s/40 s. The DZ was held at room temperature and the EG was kept in an external reservoir set to 90 °C while the oxidizing manifold was held at 120 °C. The number of MLD cycles was adjusted to produce different thicknesses of zincone films. For comparison, ALD-ZnO was deposited on a silicon electrode using DZ (Zn(C$_2$H$_5$)$_2$) and water (H$_2$O) as precursors with a pulse–purge–pulse–purge program of 0.01 s/40 s/0.01 s/40 s. Based on previous experience, 20 cycles of ALD-ZnO deposition, corresponding to a thickness of ≈3 nm were performed.

Characterization: Powder XRD patterns were analyzed on a Bruker D8 X-ray diffractometer equipped with Cu Kα ($\lambda = 1.5406$ Å) radiation. The morphology of the electrode was characterized using a Hitachi S-4800 field emission SEM, a Hitachi 3400N environmental SEM and a high-resolution TEM (JEOL 2010 FEG) equipped with an energy-dispersive X-ray spectrometer. XPS was performed using a monochromatic Al Kα source (1486.6 eV) in a Kratos AXIS Nova Spectrometer. TOF-SIMS tests were conducted using a TOF-SIMS IV machine (ION-TOF GmbH, Germany) with a 25 keV bismuth liquid metal ion source with a base pressure of $\approx10^{-8}$ mbar in the analysis chamber. For XPS and TOF-SIMS tests, the cycled silicon electrodes were washed with the dimethyl carbonate (DMC) solvent. Negative secondary ions were induced by primary ion beam bombardment of the silicon electrode surface after cycling. Zinc K-edge X-ray absorption fine structure data were collected at the hard X-ray micro analysis beamline of the Canadian Light Source.

Electrochemical Measurement: The silicon electrodes were composed of silicon nanoparticles (<100 nm, made in Shanghai Shuitian technology co. ltd.), Surp P and Sodium carboxymethyl cellulose, in an 8:1:1 mass ratio. An aqueous slurry was applied to the copper current collector and was dried at 80 °C for 10 h. The silicon electrodes were punched into discs with a 10 mm diameter. The mass loading of the active material averaged about 1.05 mg cm^{-2}. Coin cells were assembled in an Ar filled glovebox with oxygen and water concentrations less than 1 ppm using lithium metal foil as the counter electrode. 1 M LiPF$_6$ electrolyte in an EC/DMC (1:1 v/v) solvent containing 5 v% FEC was used. The ether-based electrolyte used was 1 M LiTFSI in a well-mixed solution of DME/DOL (1:1 v/v). CV measurements were carried out on a versatile multichannel potentiation 3/Z (VMP3) between 0.01 and 1.50 V at a scan rate of 0.15 mV s^{-1}. EIS was performed using the VMP3 from 0.01 to 1×10^5 Hz. For the full cell, the LiFePO$_4$ powder was used as the cathode material, with a cathode composition of 80 wt% LiFePO$_4$ powder, 10 wt% polyvinylidene fluoride and 10 wt% acetylene black. The area capacity ratio of the Si@10-ZC electrode and the LiFePO$_4$ electrode was 1.10. LiFePO$_4$//Si@10-ZC cells were tested between 2.5 and 4.1 V. All electrochemical performance testing was conducted at room temperature.

Supporting Information

Supporting Information is available from the Wiley Online Library or from the author.

Conflict of Interest

The authors declare no conflict of interest.

Data Availability Statement

Research data are not shared.

[1] Y. Cao, M. Li, J. Lu, J. Liu, K. Amine, *Nat. Nanotechnol.* **2019**, *14*, 200.

[2] T.-w. Kwon, J. W. Choi, A. Coskun, *Joule* **2019**, *3*, 662.

[3] S.-H. Park, P. J. King, R. Tian, C. S. Boland, J. Coelho, C. Zhang, P. McBean, N. McEvoy, M. P. Kremer, D. Daly, J. N. Coleman, V. Nicolosi, *Nat. Energy* **2019**, *4*, 560.

[4] T. Mu, P. Zuo, S. Lou, Q. Pan, Q. Li, C. Du, X. Gao, X. Cheng, Y. Ma, G. Yin, *Chem. Eng. J.* **2018**, *341*, 37.

[5] L. Zhang, C. Wang, Y. Dou, N. Cheng, D. Cui, Y. Du, P. Liu, M. Al-Mamun, S. Zhang, H. Zhao, *Angew. Chem., Int. Ed.* **2019**, *58*, 8824.

[6] a) G. Zhu, F. Zhang, X. Li, W. Luo, L. Li, H. Zhang, L. Wang, Y. Wang, W. Jiang, H. K. Liu, S. X. Dou, J. Yang, *Angew. Chem.* **2019**, *58*, 6669; b) S. Chen, Z. Chen, X. Xu, C. Cao, M. Xia, Y. Luo, *Small* **2018**, *14*, 1703361.

**ADVANCED
SCIENCE NEWS**

www.advancedsciencenews.com

**ADVANCED
FUNCTIONAL
MATERIALS**

www.afm-journal.de

[7] a) H. Zhang, P. Zong, M. Chen, H. Jin, Y. Bai, S. Li, F. Ma, H. Xu, K. Lian, *ACS Nano* **2019**, *13*, 3054; b) R. Shao, J. Niu, F. Zhu, M. Dou, Z. Zhang, F. Wang, *Nano Energy* **2019**, *63*, 103824.

[8] a) J. Ryu, J. H. Seo, G. Song, K. Choi, D. Hong, C. Wang, H. Lee, J. H. Lee, S. Park, *Nat. Commun.* **2019**, *10*, 2351; b) M. Chen, B. Li, X. Liu, L. Zhou, L. Yao, J. Zai, X. Qian, X. Yu, *J. Mater. Chem. A* **2018**, *6*, 3022.

[9] a) C. Wang, H. Wu, Z. Chen, M. T. McDowell, Y. Cui, Z. Bao, *Nat. Chem.* **2013**, *5*, 1042; b) J. Lopez, D. G. Mackanic, Y. Cui, Z. Bao, *Nat. Rev. Mater.* **2019**, *4*, 312; c) Q. Huang, J. Song, Y. Gao, D. Wang, S. Liu, S. Peng, C. Usher, A. Goliaszewski, D. Wang, *Nat. Commun.* **2019**, *10*, 5586.

[10] a) Y. Jin, N. H. Kneusels, L. E. Marbella, E. Castillo-Martinez, P. Magusin, R. S. Weatherup, E. Jonsson, T. Liu, S. Paul, C. P. Grey, *J. Am. Chem. Soc.* **2018**, *140*, 9854; b) Q. Li, X. Liu, X. Han, Y. Xiang, G. Zhong, J. Wang, B. Zheng, J. Zhou, Y. Yang, *ACS Appl. Mater. Interfaces* **2019**, *11*, 14066.

[11] a) Y. Jin, S. Zhang, B. Zhu, Y. Tan, X. Hu, L. Zong, J. Zhu, *Nano Lett.* **2015**, *15*, 7742; b) B. Zhu, Y. Jin, Y. Tan, L. Zong, Y. Hu, L. Chen, Y. Chen, Q. Zhang, J. Zhu, *Nano Lett.* **2015**, *15*, 5750.

[12] W. Luo, X. Chen, Y. Xia, M. Chen, L. Wang, Q. Wang, W. Li, J. Yang, *Adv. Energy Mater.* **2017**, *7*, 1701083.

[13] a) Z. Zeng, V. Murugesan, K. S. Han, X. Jiang, Y. Cao, L. Xiao, X. Ai, H. Yang, J.-G. Zhang, M. L. Sushko, J. Liu, *Nat. Energy* **2018**, *3*, 674; b) Z. Xu, J. Yang, H. Li, Y. Nuli, J. Wang, *J. Mater. Chem. A* **2019**, *7*, 9432; c) Y. He, X. Yu, Y. Wang, H. Li, X. Huang, *Adv. Mater.* **2011**, *23*, 4938.

[14] a) J. Zhang, S. Fan, H. Wang, J. Qian, H. Yang, X. Ai, J. Liu, *ACS Appl. Mater. Interfaces* **2019**, *11*, 13251; b) S. Zeng, D. Liu, Y. Chen, J. Qian, Y. Cao, H. Yang, X. Ai, *J. Mater. Chem. A* **2015**, *3*, 9938; c) M.-S. Song, G. Chang, D.-W. Jung, M.-S. Kwon, P. Li, J.-H. Ku, J.-M. Choi, K. Zhang, G.-R. Yi, Y. Cui, J. H. Park, *ACS Energy Lett.* **2018**, *3*, 2252.

[15] a) Y. Zhao, X. Sun, *ACS Energy Lett.* **2018**, *3*, 899; b) C. Ban, S. M. George, *Adv. Mater. Interfaces* **2016**, *3*, 1600762.

[16] a) D. M. Piper, J. J. Travis, M. Young, S. B. Son, S. C. Kim, K. H. Oh, S. M. George, C. Ban, S. H. Lee, *Adv. Mater.* **2014**, *26*, 1596; b) Y. Ma, J. M. Martinez de la Hoz, I. Angarita, J. M. Berrio-Sanchez, L. Benitez, J. M. Seminario, S. B. Son, S. H. Lee, S. M. George, C. Ban, P. B. Balbuena, *ACS Appl. Mater. Interfaces* **2015**, *7*, 11948;

c) S. B. Son, Y. Wang, J. Xu, X. Li, M. Groner, A. Stokes, Y. Yang, Y. T. Cheng, C. Ban, *ACS Appl. Mater. Interfaces* **2017**, *9*, 40143.

[17] C. Zhu, K. Han, D. Geng, H. Ye, X. Meng, *Electrochim. Acta* **2017**, *251*, 710.

[18] B. Yoon, B. H. Lee, S. M. George, *J. Phys. Chem. C* **2012**, *116*, 24784.

[19] T. T. H. Hoang, S. Ma, J. I. Gold, P. J. A. Kenis, A. A. Gewirth, *ACS Catal.* **2017**, *7*, 3313.

[20] M. Aghaee, J. P. Niemela, W. M. M. Kessels, M. Creatore, *Dalton Trans.* **2019**, *48*, 3496.

[21] B. Yoon, J. L. O'Patchen, D. Seghete, A. S. Cavanagh, S. M. George, *Chem. Vap. Deposition* **2009**, *15*, 112.

[22] J. H. Lin, R. A. Patil, R. S. Devan, Z. A. Liu, Y. P. Wang, C. H. Ho, Y. Liou, Y. R. Ma, *Sci. Rep.* **2014**, *4*, 6967.

[23] T. Mu, B. Shen, S. Lou, Z. Zhang, Y. Ren, X. Zhou, P. Zuo, C. Du, Y. Ma, H. Huo, G. Yin, *Chem. Eng. J.* **2019**, *375*, 121923.

[24] P. Fan, S. Lou, B. Sun, L. Wu, Z. Qian, T. Mu, Y. Ma, X. Cheng, Y. Gao, P. Zuo, C. Du, G. Yin, *Electrochim. Acta* **2020**, *332*, 135507.

[25] P. Fan, T. Mu, S. Lou, X. Cheng, Y. Gao, C. Du, P. Zuo, Y. Ma, G. Yin, *Electrochim. Acta* **2019**, *306*, 590.

[26] T. Mu, Z. Zhang, Q. Li, S. Lou, P. Zuo, C. Du, G. Yin, *J. Colloid Interface Sci.* **2019**, *555*, 783.

[27] X. Zhou, Y. Liu, C. Du, Y. Ren, T. Mu, P. Zuo, G. Yin, Y. Ma, X. Cheng, Y. Gao, *J. Power Sources* **2018**, *381*, 156.

[28] J. Liang, X. Li, Y. Zhu, C. Guo, Y. Qian, *Nano Res.* **2014**, *8*, 1497.

[29] B. Li, S. Li, J. Xu, S. Yang, *Energy Environ. Sci.* **2016**, *9*, 2025.

[30] a) J. Zhou, S. Jiang, Y. Li, Z. Pan, Y. Qian, Y. Zhao, N. Lin, Y. Qian, *Energy Storage Mater.* **2020**, *31*, 36; b) H. Liu, X. Liu, W. Li, X. Guo, Y. Wang, G. Wang, D. Zhao, *Adv. Energy Mater.* **2017**, *7*, 1700283; c) X. Tang, X. Guo, W. Wu, G. Wang, *Adv. Energy Mater.* **2018**, *8*, 1801897.

[31] A. K. Yadav, R. Dey, S. N. Jha, D. Bhattacharyya, S. Hussain, R. Bhar, A. K. Pal, *X-Ray Spectrom.* **2018**, *47*, 484.

[32] C. Xu, F. Lindgren, B. Philippe, M. Gorgoi, F. Björefors, K. Edström, T. Gustafsson, *Chem. Mater.* **2015**, *27*, 2591.

[33] a) J. Zhao, L. Liao, F. Shi, T. Lei, G. Chen, A. Pei, J. Sun, K. Yan, G. Zhou, J. Xie, C. Liu, Y. Li, Z. Liang, Z. Bao, Y. Cui, *J. Am. Chem. Soc.* **2017**, *139*, 11550; b) B. H. Shen, S. Wang, W. E. Tenhaeff, *Sci. Adv.* **2019**, *5*, eaaw4856.

[34] C. Zhao, C. Yu, B. Qiu, S. Zhou, M. Zhang, H. Huang, B. Wang, J. Zhao, X. Sun, J. Qiu, *Adv. Mater.* **2018**, *30*, 1702486.